Weierstraß-Institut
für Angewandte Analysis und Stochastik

im Forschungsverbund Berlin e.V.

Preprint ISSN 0946 – 8633

Flow solution properties in full-zone thermocapillary liquid bridges

D. A. R. Davis [1], F. T. Smith [2]

submitted: 25th May 2004

[1] Weierstrass Institute
for Applied Analysis
and Stochastics,
Mohrenstraße 39,
D - 10117 Berlin, Germany.
E-Mail: davis@wias-berlin.de

[2] Department of Mathematics,
University College London,
Gower Street, London.
WC1E 6BT.
England, UK.
E-Mail: frank@math.ucl.ac.uk

No. 936
Berlin 2004

2000 *Mathematics Subject Classification.* 35B40, 53A05, 65M60, 76D05, 76E30.

Key words and phrases. liquid bridges, floating-zone, thermocapillarity, finite-element, Navier–Stokes equations, transient, three-dimensional, mode interaction, nonlinearity, midzone.

Edited by
Weierstraß-Institut für Angewandte Analysis und Stochastik (WIAS)
Mohrenstraße 39
10117 Berlin
Germany

Fax: + 49 30 2044975
E-Mail: preprint@wias-berlin.de
World Wide Web: http://www.wias-berlin.de/

Abstract

Properties of low Prandtl number flows in slender cylindrical liquid bridges driven by interfacial thermocapillary forces are addressed here in a theoretical and computational light. Both 'outward' (positive Marangoni number Ma) and 'inward' (negative Ma) flow along the liquid-gas interface are considered. In previous investigations (Davis & Smith 2003), a solution curve for steady, axisymmetric flow was determined from asymptotic theory in the context of slender bridges. It indicated both the non-existence of solutions beyond a positive, cut-off value of the scaled Marangoni number and a double branch in the case of solvability (although with only one 'attractor'). In the present study full numerical simulation (using a finite-element iterative solver, described herein) reveals the unsteady, three-dimensional nature of the flow solution beyond the cut-off value. Attention is paid to the case where the radius-to-height aspect ratio is 0.5, from which the (nonlinearly-coupled) azimuthal modes m=1 and m=2 are seen to dominate. The branch behaviour is then examined for $Ma < 0$, and asymptotic analysis reveals that a critical value of the scaled Marangoni number exists, on approach to which the pressure gradient across the midzone becomes large and negative. Full computational solutions on the attractor branch for $Ma < 0$ are subsequently presented, and these show encouraging agreement with asymptotic predictions (as well as slender-flow midzone computations) near the critical Marangoni number. The critical value moreover is shown to correspond to the onset of 'lemonheads' (non-convex radial velocity profiles near the midzone), in precisely the same manner as the cut-off value for positive Ma.

1 Introduction

Thermocapillary flows feature in a wide range of physical systems and technical processes. Furthermore, as Davis (1987) points out there are a significant class of problems where the thermocapillarity dominates the dynamics, such as in the behaviour of weld pools, the rupture of thin films, the movement of contact lines, the propagation of flames over liquid fuels and the containerless processing of crystals. We are especially interested in the last application, at least for low Prandtl number flows, although we don't restrict ourselves completely to crystal growth; more generally we are concerned with understanding the structure and dynamics of liquid bridges, as well as identifying key parameter values marking the onset of major structural changes within the flow.

Instabilities in thermocapillary liquid bridges have been of interest in recent years, due in part to the direct applicability to floating-zone crystal growth processes. For low Prandtl numbers (Pr) this applies to semiconductor melts, e.g. silicon ($Pr = 0.01$), morybdenum ($Pr = 0.025$) or gallium arsenide ($Pr = 0.068$). The stability nature of such flows is a subject of great importance in the crystal growth industry. Experimental studies (e.g. Chun & Wuest 1979, Preisser, Schwabe & Scharmann 1983, Hu, You & Cao 1992) have clearly identified two distinct types of instability which are exclusively relevant to low Prandtl number flows: firstly, steady axisymmetric flow was seen to undergo transition to a *stationary*, three-dimensional (3D) state at a critical Marangoni number (Ma), say Ma^{c_1}, and secondly, at a higher value Ma^{c_2} the flow becomes unstable to (3D) *oscillatory* instabilities. A common feature of the latter instability type was the observation of unwanted striations in the finished crystal, which was not really observed for the first instability type (see also Eyer, Leiste & Nitsche 1985, Jurisch & Löser 1990). As noted in Wanschura *et al.* 1995 however, for both types of stability "the detailed structure of the disturbance flow and its azimuthal wavenumber remained largely unknown, due to the experimental difficulties associated with the flow and temperature measurements in small liquid volumes". (The smallness of the liquid volume is of course a necessary condition in a terrestrial environment – in which the give experiments were performed – to ensure the liquid bridge doesn't collapse. It also serves to reduce buoyancy effects.) Hence, numerical simulation (especially when coupled with mathematical results from reduced models) can be of great value in understanding the instabilities more precisely.

Numerical linear instability analysis for problems with and without significant buoyancy present

have allowed a better understanding of the underlying mechanisms leading to both types of instability, as well as identifying the most dangerous linear azimuthal mode, in each case. For pure thermocapillarity, on which we concentrate in this paper, these include studies by Levenstam & Amberg 1995, Wanschura *et al.* 1995, Leypoldt, Kuhlmann & Rath 2000. In particular, it was demonstrated that the stationary instability is essentially hydrodynamic in nature. Consequently, for Marangoni numbers beyond this critical bifurcation value, the flow is time-dependent on a timescale that scales with $Ma/(Ma - Ma^{c_1})$. We emphasise here however, that these results apply to the related but nevertheless distinct 'half-zone' problem, where simplified boundary conditions are applied to 'approximate' the upper or lower half of a non-deformed (i.e. cylindrical), floating-zone configuration. For full zones very little has been demonstrated in this context; Kaiser & Benz (1998) show that the two instability types occur for full zones via direct numerical simulation, and predict the corresponding Marangoni numbers (which agree well with experimental results); however the mode behaviour itself, even linear aspects, are not considered.

In this first part of this paper we concentrate in detail on the first instability type, since we feel that, despite a generally thorough understanding of the basic linear properties, from half-zone work at least, very little is known on weakly-nonlinear aspects of the instability, i.e. mode interaction, for either full zones or half zones. For this purpose we computed weakly-supercritical flow via full numerical simulation, using a transient, 3D finite-element solver, and here we analyse some of the cases.

Negative Marangoni numbers are also studied since, as argued in Davis & Smith 2003 (herafter referred to as DS), several situations could arise where they occur – firstly, although rare the surface-tension gradient for the liquid could be positive-valued; secondly, inhomogeneous heat-loss effects at the liquid-gas interface could conceivably induce "localised" regions with negative Marangoni number in effect - this would be particularly relevant if situated around the midheight of the domain, where strong convective processes have already been identified (DS). A third situation is with liquid cooling problems. The slender-flow work of DS revealed that two solution branches exist for negative Marangoni number, although one of these has proven to be more an exotic special case rather than having any practical relevance, i.e. it has not been possible to compute solutions for this branch via full numerical simulation (using a similar solver to the one described in this paper). The reduced-model computational results in DS suggested that the branches 'cut out' at finite scaled values of the Marangoni numbers where the pressure becomes large and negative, and this is confirmed in the present work for the 'attractor' branch, using asymptotic analysis, where good agreement with computational solutions is seen to occur.

The paper is structured as follows. In Section 2 we introduce the controlling hydrothermal system of equations, and a description of the main parameters in the problem. Then in Section 3 details of the computational solution method used for full numerical simulation are given, while in Section 4 results for three-dimensional weakly-supercritical flow (positive Ma) are presented. Here dominant frequencies and mode interactions are analysed. The slender-flow system of equations holding around the midheight of the domain, which was first derived in DS, is addressed theoretically in Section 5, and an asymptotic form for the ultimate behaviour of the attractor branch for negative Ma is established. In Section 6, steady axisymmetric numerical results for $Ma < 0$ are presented, and comparisons are made with reduced-model computations as well as the theoretical predictions of Section 5. Finally conclusions are made in Section 7.

2 The governing system of equations

Following the analysis and arguments in DS, we wish to solve a system comprising the incompressible Navier-Stokes equations and the heat-transport equation in a cylindrical domain, and having

the dimensionless form:

$$\frac{\partial \boldsymbol{u}}{\partial t} + (\boldsymbol{u}\cdot\boldsymbol{\nabla})\boldsymbol{u} - \Delta\boldsymbol{u} + \boldsymbol{\nabla}p = \boldsymbol{0} \ \text{ in } \ \Omega, \tag{2.2a}$$

$$\boldsymbol{\nabla}\cdot\boldsymbol{u} = 0 \ \text{ in } \ \Omega, \tag{2.2b}$$

$$\frac{\partial T}{\partial t} + (\boldsymbol{u}\cdot\boldsymbol{\nabla})T - \frac{1}{Pr}\Delta T = 0 \ \text{ in } \ \Omega. \tag{2.2c}$$

Here $\boldsymbol{u}$, p and T denote the *dimensionless* velocity, pressure and temperature fields, respectively, while Ω represents the dimensionless (cylindrical) cavity. The associated boundary conditions are

$$\boldsymbol{u} = 0, \ T = 0 \ \text{ on } \ \Gamma_{SL}, \tag{2.2d}$$

$$\boldsymbol{u}\cdot\boldsymbol{n} = 0, \ T = T_D \ \text{ on } \ \Gamma_{LG}, \tag{2.2e}$$

$$\boldsymbol{n}\cdot\sigma\boldsymbol{\tau} = -\frac{Ma}{Pr}\boldsymbol{\nabla}T\cdot\boldsymbol{\tau} \ \text{ on } \ \Gamma_{LG}, \tag{2.2f}$$

where $\sigma \equiv \boldsymbol{\nabla}\boldsymbol{u} + \boldsymbol{\nabla}\boldsymbol{u}^{\mathrm{T}} - p\mathrm{I}_3$ denotes the stress tensor, with superscript T indicating the transpose and I_3 the 3×3 identity (delta) tensor. Also here Γ_{SL}, Γ_{LG} are the solid/liquid and liquid/gas boundaries (both dimensionless), in turn, T_D is the scaled external temperature imposed on the free surface, $\boldsymbol{\tau}$ is an arbitrary vector in the local tangential plane to Γ_{LG}, and $\boldsymbol{n}$ is the normal vector to Γ_{LG} (see Figure 1). In parametric form, the surfaces Γ_{SL}, Γ_{LG} can be expressed as:

$$\Gamma_{SL} = \big\{(r,z,\theta)|r\in[0,rc], \ z\in\{0,1\}, \ \theta\in[0,2\pi)\big\}, \tag{2.2g}$$

$$\Gamma_{LG} = \big\{(r,z,\theta)|r\in\{rc\}, \ z\in[0,1], \ \theta\in[0,2\pi)\big\}, \tag{2.2h}$$

where rc denotes the dimensionless radius of the cylinder.

Finally, initial conditions

$$\boldsymbol{u} = \boldsymbol{u}_0, \ T = T_0 \ \text{ in } \Omega \ \text{ at } \ t = 0 \tag{2.2i}$$

are required to close the system.

In the above derivation, we have assumed negligible buoyancy effects as well as high surface tension and low capillary number. The last two assumptions, as explained in DS, allow us to approximate the liquid-gas interface by a non-deformable, cylindrical surface.

Solutions of (2.2a–f,i) are then sought for various values of the Marangoni number Ma, while the Prandtl number Pr is held fixed. A small Prandtl number is selected since this is directly relevant for several applications of interest to us, e.g. in semiconductor crystal growth, the Prandtl number typically has values lying in the range 0.01 to 0.08. Consequently, under moderate conditions, there is little feedback from the velocity on the temperature via advection, a feature that has been exploited in the steady axisymmetric slender-flow modelling of (2.2a–f) (DS). There, the problem reduces to a hydrodynamic system, where a strong convective mechanism occurring at the midzone was identified(see also Section 5). Hence, we concentrate on flow aspects in the subsequent sections.

3 Variational equations and computational method

For both steady and unsteady flow, the same transient solver is applied; in the former case, we consider a solution as being obtained, once a sufficiently small tolerance value, measuring the $L_2(\Omega)$

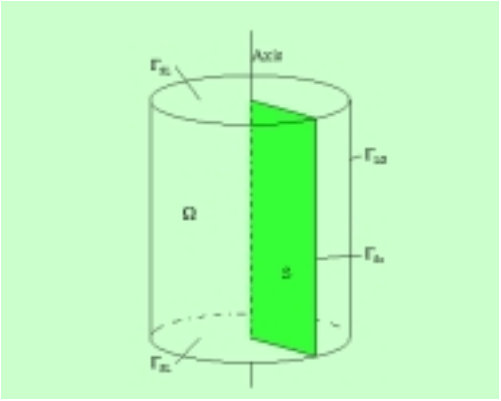

(a)

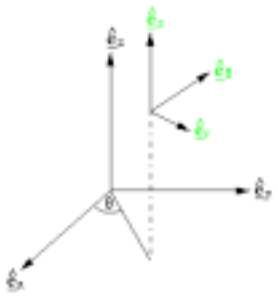

(b)

Figure 1: (a) Sketch of a cylindrical liquid-bridge domain Ω, with solid-liquid boundaries Γ_{SL} and liquid-gas interface Γ_{LG}. For two-dimensional flow computation, axisymmetric solutions are sought in an arbitrary vertical 'slice' S (with liquid-gas interface Γ_{S_0}). (b) Cylindrical and Cartesian coordinate systems.

norm of the solution difference between successive time steps, is reached, and remains below this value for a sufficiently long time interval.

For the spatial discretisation, a standard Bubnov–Galerkin finite-element method was used. In contrast to the axisymmetric computational approach (see DS for details), where (2.2*a–f*) are converted into a variational form, which can directly accommodate the stress condition on the slip boundary, we choose to apply the conventional Gaussian approach to the integration of the diffusion term, leading to the form:

$$\frac{\mathrm{d}}{\mathrm{d}t}\int_\Omega \boldsymbol{u}\cdot\boldsymbol{\phi}\; d\mathbf{x} + \int_\Omega \nabla(\boldsymbol{u}) : \nabla\boldsymbol{\phi}\; d\mathbf{x} + \int_\Omega [(\boldsymbol{u}\cdot\boldsymbol{\nabla})\boldsymbol{u}]\cdot\boldsymbol{\phi}\; d\mathbf{x}$$

$$- \int_\Omega p\boldsymbol{\nabla}\cdot\boldsymbol{\phi}\; d\mathbf{x} - I_\Gamma = 0, \tag{3.1a}$$

$$\int_\Omega (\boldsymbol{\nabla}\cdot\boldsymbol{u})\psi\; d\mathbf{x} = 0, \tag{3.1b}$$

$$\frac{\mathrm{d}}{\mathrm{d}t}\int_\Omega T\chi\; d\mathbf{x} + \int_\Omega [(\boldsymbol{u}\cdot\boldsymbol{\nabla})T]\chi\; d\mathbf{x} + \frac{1}{Pr}\int_\Omega \boldsymbol{\nabla}T\cdot\boldsymbol{\nabla}\chi\; d\mathbf{x} = 0, \tag{3.1c}$$

where $\mathbf{u}\in\mathbf{X} := \{\mathbf{v}\in(\mathbf{H}_1(\Omega))^3 : \mathbf{v}=0 \text{ on } \delta\Omega\setminus\Gamma_{LG},\ \mathbf{v}\cdot\mathbf{n}=0 \text{ on } \Gamma_{LG}\}$, $p\in Y := L_2(\Omega)\setminus\mathbb{R}$, $T\in Z := H_1(\Omega)$, and the test functions $\boldsymbol{\phi}$, ψ, χ belong to the spaces $\mathbf{X}$, Y, Z, respectively. Also, we require $\mathbf{u}=\mathbf{u}_0$, and $T=T_0$ at $t=0$, and note that $\mathbf{u}_0$ should be divergent-free in Ω and have continuous normal component (zero, for the problem in hand) on all Dirichlet boundary portions (Gresho & Sani 2000). Here

$$I_\Gamma := \int_{\Gamma_{LG}} \frac{\partial\boldsymbol{u}}{\partial n}\cdot\boldsymbol{\phi}\; ds \tag{3.2}$$

denotes the boundary-integral contribution along the liquid–gas interface. As shown more generally in Appendix A, it is possible to accommodate the tangential stress boundary condition (2.2f), by converting (3.2) into an equivalent stress-curvature-torsion (SCT) form; furthermore using extreme

normal curve sections, which are (uniquely) $\boldsymbol{\tau}_1 = \hat{e}_z$ and $\boldsymbol{\tau}_2 = \hat{e}_\theta$ for the cylindrical surface considered, it follows immediately from (A13) that

$$I_\Gamma = -2\pi r_c \left(\frac{Ma}{Pr}\right) \int_0^1 (\boldsymbol{\phi} \cdot \hat{e}_z) \frac{dT_D}{dz} dz + 2\pi \int_0^1 (\boldsymbol{\phi} \cdot \hat{e}_z)(\mathbf{u} \cdot \hat{e}_z) dz, \tag{3.3}$$

since the curvature values 0, r_c^{-1} apply to $\hat{e}_z$, $\hat{e}_\theta$ respectively.

Discrete solutions $\mathbf{u_h} \in \mathbf{X}_h$, $p_h \in Y_h$, $T_h \in Z_h$ are sought, such that (3.1a-c) hold for all $\boldsymbol{\phi} \in \mathbf{X}_h$, $\psi \in Y_h$, $\chi \in Z_h$, respectively. Here $\mathbf{X}_h$, Y_h, Z_h are determined by the finite element under consideration. In our applications here, the Taylor–Hood triangular element has been implemented, and hence, the velocity and temperature spaces comprise continuous, piecewise-quadratic polynomials, while continuous, piecewise-linear polynomials form a basis for the discrete pressure space. For this element, the velocity and temperature are of third-order spatial accuracy, while the pressure is of second-order spatial accuracy (in each case measured by the $L^2(\Omega)$ norm).

To discretise in time, a fractional-θ scheme with operator splitting as variant (Bänsch 1998; Bristeau, Glowinski & Periaux 1987) was applied to the hydrodynamic part combined with a Crank-Nicolson scheme for the energy equation. The essential feature of the former scheme is the numerical decoupling of the nonlinearity and incompressibility as described in detail in DS; there descriptions of the methods used to solve the subsequent matrix systems are also given (see also Davis & Bänsch 2002).

4 Numerical results for $Ma > 0$

In DS two-dimensional axisymmetric steady solutions were computed in the context of narrow domains, amongst other possibilities, and for low Prandtl numbers. The flow solution in this instance is characterised by two co-axial counter-rotating vortices of equal size which meet at the midheight. Both full numerical solutions based on solving (2.2a–f,i) via a finite-element scheme, and numerical solutions based on solving an asymptotic nonlinear–viscous slender-flow model with $rc \ll 1$ and $Pr \ll 1$ were obtained. The latter showed that steady axisymmetric solutions cease to exist when the scaled thermocapillary parameter AM (explicitly defined in Section 5 below) exceeds a value AML (≈ 3.3108).

Given the known findings from the related half-zone problem (Levenstam & Amberg 1995, Wanschura *et al.* 1995), we anticipated that for $AM > AML$ three-dimensionality would play a rôle, not only for narrow domains, but all possible cylindrical aspect ratios. The latter reference suggests further that the most dangerous linear mode m increases with rc, via the (heuristic) approximate relationship $m = 4\,rc$; interestingly, Levenstam and Amberg suggested that the instability can be compared to that of a vortex ring of constant vorticity in an ideal fluid, for which Widnall & Tsai (1977) formally determined the relationship $m = 5\,rc$.

Motivated by the reduced-model findings and half-zone results, three-dimensional transient simulations, based on using the numerical method outlined in the previous section, were performed for a number of cases. Owing in part to the increased difficulty of performing three-dimensional simulations with narrow domains, especially regarding problems with grid resolution, we chose a moderately small value namely $rc = 0.5$; this value of rc is also more typical for a real crystal-growth float-zone experiment, for example. In addition, the Prandtl number was fixed to be 0.02,

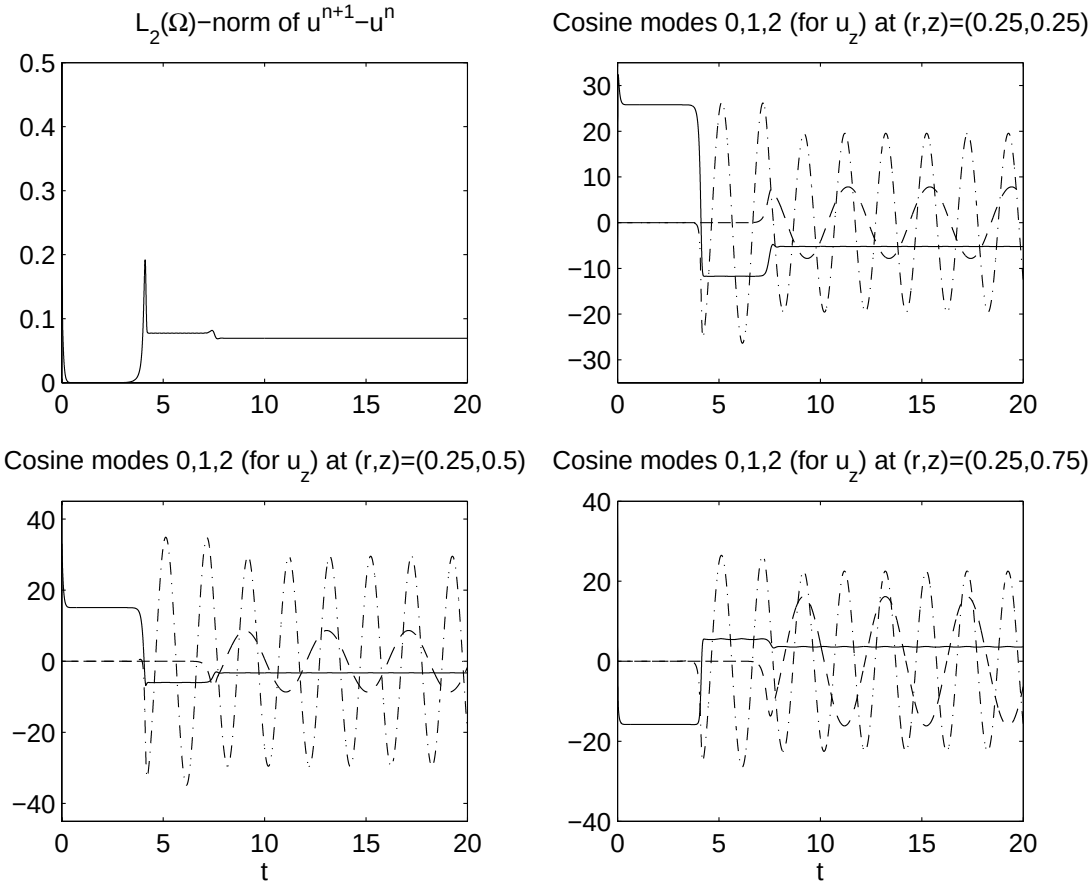

Figure 2: Three-dimensional flow simulation for $Re_D = 2500$, $Pr = 0.02$, $rc = 0.5$ depicting the time histories of (a) the $L_2(\Omega)$-norm of successive velocity solutions; (b),(c),(d) the cosine modes $m = 0$ (–),1 (- -), 2 (- .) of the axial velocity component at $(r, z) = (0.25, 0.25)$, $(0.25, 0.5)$, $(0.25, 0.75)$, in turn.

while the initial solution was taken to be either a solution at a lower Marangoni number or else $\mathbf{u}_0 = \mathbf{0}$, $T_0 = T_c$; here T_c denotes the steady heat-conduction profile obtained by solving (2.2c–e,i) without advection in the first equation.

The sample of results presented here were all obtained using a tetrahedral mesh comprising 31620 elements, 44135 velocity/temperature nodes and 5778 pressure nodes. The timestep size varied between 0.0005 and 0.001. All results were fully converged with respect to mesh refinement and timestep size. In the following we consider the four cases Re_D=2500,2600,2700,2800, where $Re_D \equiv Ma/Pr$ defines the *dynamic Reynolds number*, concentrating mainly on the first case. Before discussing these, we note that solutions were also obtained for Re_D values up to and including 2400, and for comparable mesh and timestep sizes; all of these yielded steady state solutions.

An unsteady solution is first obtained for $Re_D = 2500$, and as expected three-dimensionality is found to play a central rôle; before discussing this further, it is convenient here to introduce the following representation for the axial velocity component $u_z := \mathbf{u} \cdot \hat{\mathbf{e}}_z$ via cylindrical coordinates (r, z, θ) (see Figure 1(b)):

$$u_z = a_0(r, z, t) + \sum_{m=1}^{\infty} a_m(r, z, t) \cos(m\theta) + \sum_{m=1}^{\infty} b_m(r, z, t) \sin(m\theta), \tag{4.1}$$

where a_m and b_m denote the m'th Fourier cosine and sine mode in turn, while c.c. stands for complex conjugate. We note that the form of (4.1) is valid for all the pointwise-defined flow quantities, but that we have chosen to concentrate on just one of these.

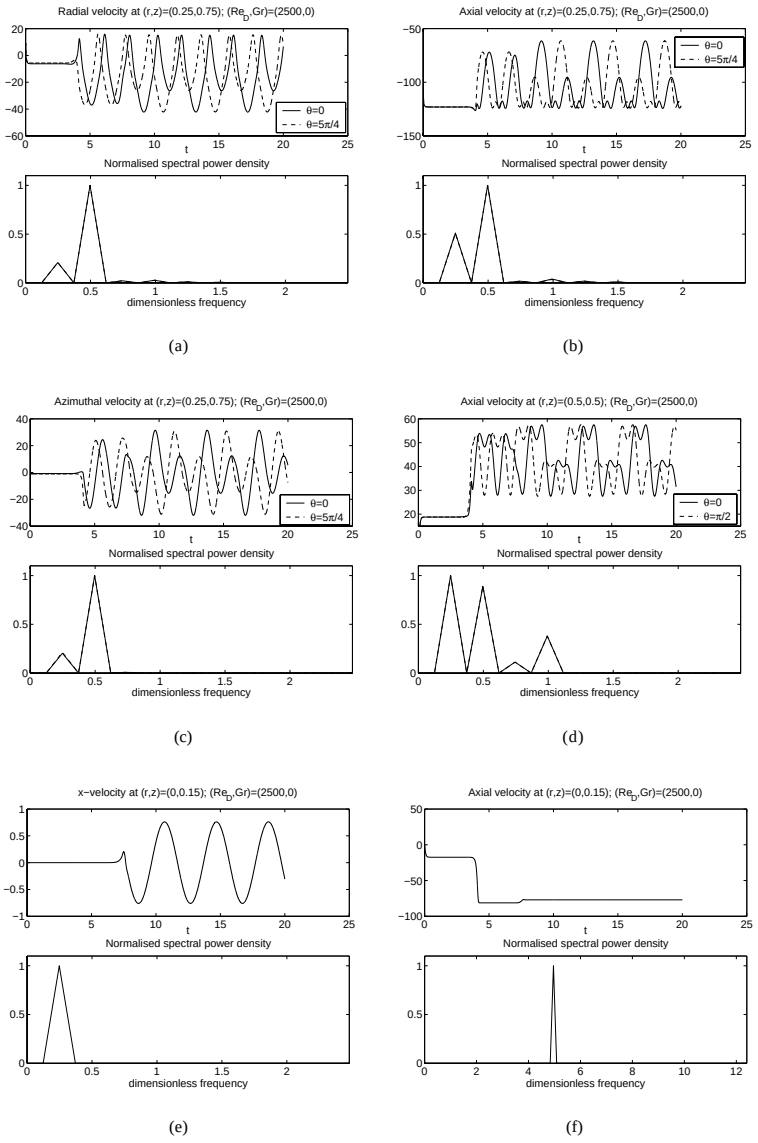

Figure 3: Time history behaviour and associated normalised frequency spectra for $Re_D = 2500$, $Pr = 0.02$, $rc = 0.5$ showing (a),(b),(c) radial, axial, azimuthal velocity components in turn at $(r, z, \theta) = (0.25, 0.75, 0)$, $(0.25, 0.75, 5\pi/4)$; (d) axial velocity component at $(r, z, \theta) = (0.5, 0.5, 0)$, $(0.5, 0.5, \pi/2)$; (e),(f) x-, axial velocity components at $(r, z) = (0, 0.15)$. In plots (a)-(d), the frequency spectra for both curves are identical.

The time histories for the three modes m =0, 1 and 2 are displayed in Figure 2, along with a plot indicating the norm of the difference of successive solutions. We note here that all modes of higher value are subdominant. The three modes are depicted along three circular curves, from which several distinct features can be discerned. Firstly, it is clear that the $m = 2$ mode is the

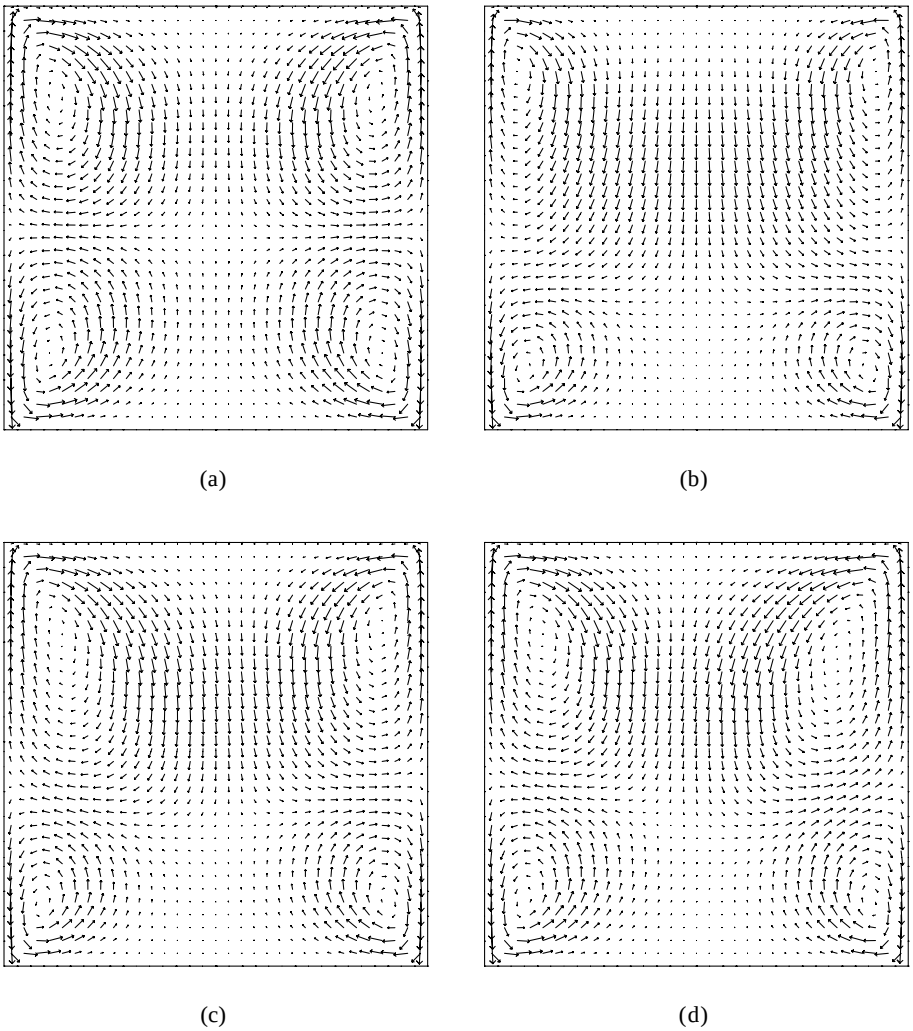

Figure 4: Computed transient velocity field for $Re_D = 2500$ $Pr = 0.02$, $rc = 0.5$ at the dimensionless times (a) 2.2; (b) 6.2; (c) 10.8; (d) 17.0.

first of the 3D modes to become active and at a time $t \approx 3.9$; this remains solely dominant until $t \approx 7.5$, when the $m = 1$ mode (with frequency 0.25) starts to oscillate visibly. It is evident from Figure 2, that the $m = 2$ mode (frequency 0.50) has double the frequency of that for $m = 1$, which in turn suggests that the modes are nonlinearly coupled. While the oscillatory behaviour of most flow quantities will be determined by the frequency values of these two modes (see Figure 3) a notable exception is with quantities involving integration over a given azimuthal angle range (such as the $L_2(\Omega)$-norm of point quantities) as well as the axial velocity component along the axis; the latter has a frequency value of 5.0, which corresponds to the basic linear frequency of the $m = 0$ mode. The actual nonlinearly-affected frequency of the $m = 0$ mode is 1.0 we note, and one possibility may be that its frequency stems from mode interaction involving the $m = 2$ mode and a 'mirror' mode having the same wavenumber but an opposite sign for the frequency, although no firm evidence can be provided. It is clear however from Figure 2 that the axisymmetric mode is nonlinearly affected by the appearance of both modes, especially $m = 2$. Another interesting feature is the behaviour of u_x at the axis, where u_x defines the horizontal velocity component at the axis directed along $\theta = 0$ (i.e. $y = 0,\ x \geq 0$). From mathematical theory, coefficients of u_r and u_θ associated with *even* values of m must tend to zero on approach to the axis to avoid

Dyn. Reynolds number Re_D	dominant frequency(ies)	significant other frequencies	main 3D mode(s) near start/at end-time $t = 20$
0 – 2400	——-	——	—/—
2500	0.5	0.25; 1.0; 5.0	2/1; 2
2600	0.52	0.26; 0.78; 1.04; 5.21	2/1; 2
2700	0.28	0.56; 5.56	2/1; 2
2800	0.32	0.63; 6.27	2/1

Table 1: Frequency data for three-dimensional flow simulations with Re_D ranging from 0 to 2800. In the final column, "start" indicates the first appearance of 3D effects.

non-unique limiting values there (seen for example by imagining the velocity around an arbitrarily thin column surrounding the axis, letting the column radius shrink to zero, and using azimuthal symmetry properties for the modes in question). The odd modes (dominated by $m = 1$) naturally avoid this scenario however, and because $u_x = u_r \cos(\theta) - u_\theta \sin(\theta)$ for $r > 0$, we would also expect the frequency associated with $m = 1$ to dominate the behaviour of u_x on approach to, and at the axis; this is indeed observed in Figure 3e. We note further that u_y at the axis (defined along $\theta = \pi/2$) has analogous behaviour, but not necessarily u_z, which is unaffected by the 'thin column' argument (Figure 3f). All frequency measurements were made using Matlab's fast Fourier transform internal function, and for the time interval [10,20].

In Figure 4, results for $Re_D = 2500$ are presented indicating four different snapshots with corresponding times $t = 2.0, 6.0, 10.8$ and 17.0. The first two time instants correspond to the axisymmetric- and $m = 2$ - dominated stages of the flow development, and indicate that the upper vortex increases in size and moves below the midzone while the lower vortex correspondingly shrinks. Perspective plots (not shown) indicate that the vortices are now "saddle-shaped" (see e.g. Levenstam & Amberg 1995), in line with the dominance of the $m = 2$ mode. The final two plots show the flow behaviour once the $m = 1$ mode is fully active; here a slight loss of mirror symmetry associated with $m = 2$ can be observed.

As the value of Re_D is increased beyond 2500 however, we observe a shift in the dominance of the modes $m = 1$ and $m = 2$, as readily demonstrated in Figure 5. Correspondingly, the vortices become more skewed and mirror symmetry is completely lost, as can be readily seen in Figure 6 for two time instants. A summary of the dominant frequency behaviour for the cases considered is given in Table 1.

5 Slender-flow approximation

A hydrodynamic, slender-flow approximation of the steady axisymmetric system (based on assuming $Pr \ll 1$ and $r_c \ll 1$) was derived in DS, and subsequently solved numerically using a finite-difference scheme, with the nonlinear terms lagged and upwinded. For positive Marangoni number comparisons with full DNS (finite-element) solutions (using $Pr = 0.01$, $r_c = 0.1$) were made. Very good agreement was obtained for problems both with and without buoyancy considered; for the latter this included AM values up to and including 3, where $AM \equiv r_c^3(Ma/Pr)$ is the scaled Marangoni number in effect. The sudden non-existence of a solution beyond the value 3.3108 ($:=AML$) prompted interest in examining the flow mechanisms at the midzone ($z \approx 0.5$), as explained next.

From the subcritical numerical computations in DS it was shown that, as the thermocapillary stress on the liquid–gas interface is increased, the flow around the midheight of the domain starts

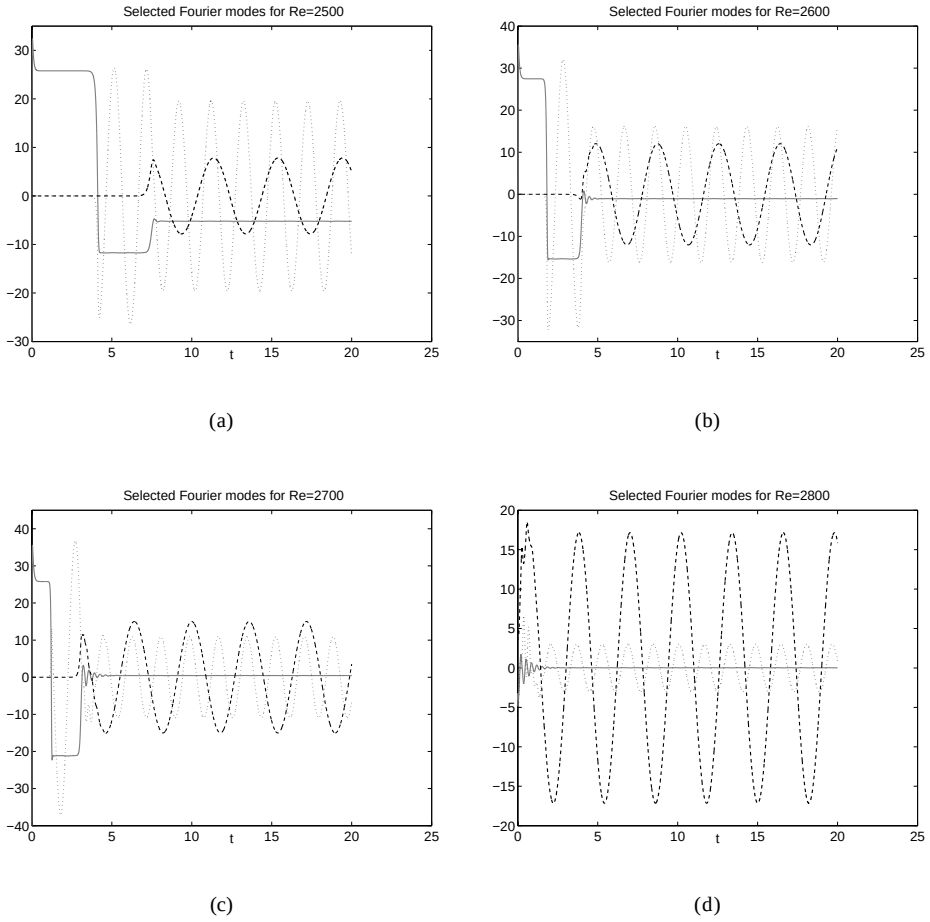

Figure 5: Time histories of the cosine modes $m = 0$ (–),1 (- -), 2 (. .) of the axial velocity component at $(r, z) = (0.25, 0.25)$ for $Pr = 0.02$, $rc = 0.05$ and (a) $Re_D = 2500$; (b) $Re_D = 2600$; (c) $Re_D = 2700$; (d) $Re_D = 2800$.

to become highly convective, almost jet-like. This makes intuitive sense when considering the fundamental form of the solution for steady, axisymmetric flows, i.e. two counterrotating tori which meet at the midheight, and increase in strength, as the Marangoni number is increased.

5.1 The midzone system

From the full numerical simulation of DS, the emergence of non-convex radial velocity profiles in the vertical direction (the so-called 'lemonheads') for relatively narrow domains was shown to coincide with the 'cut-off' value AML being exceeded in the slender-flow model. To recap, the model suggests solving an ordinary-differential, nonlinear-viscous system of the form:

$$(\bar{r}\tilde{u})' + \bar{r}\tilde{w} = 0, \quad \tilde{u}\tilde{w}' + \tilde{w}^2 = -\tilde{q} + (\bar{r}\tilde{w}')'/\bar{r}, \tag{5.1a,b}$$

around $z = 0.5$, where $\tilde{u}(\bar{r})$, $\tilde{w}(\bar{r})$ denote the *scaled* local radial and axial velocity components, $\tilde{q}$ is the scaled local constant-valued pressure gradient, and $\bar{r}$ is the scaled radial coordinate. The absence of any temperature feedback on the hydrodynamic system is a direct consequence of assuming negligible buoyancy which, as noted in DS, only first becomes significant for very high

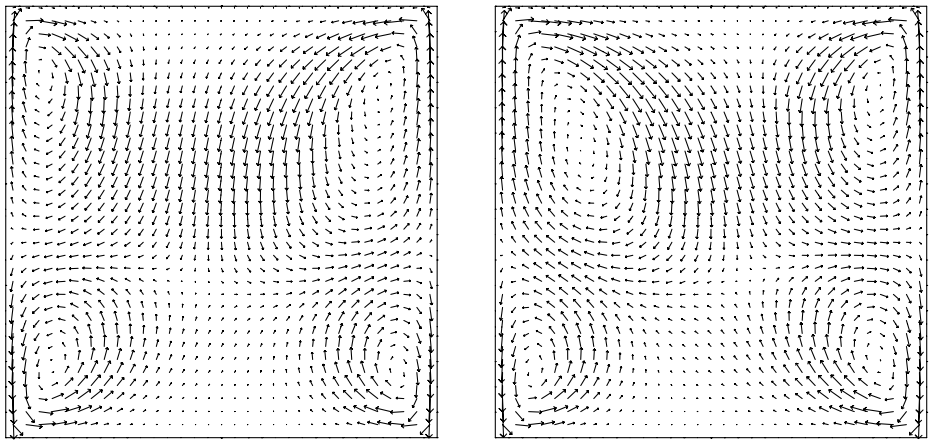

(a) (b)

Figure 6: Computed transient velocity field for $Re_D = 2800$, $Pr = 0.02$, $rc = 0.5$ at the dimensionless times (a) 8.2; (b) 13.2.

values of the Grashof number ($Gr \sim r_c^{-6}$). For the external temperature profile $T_D(z) \equiv \sin(\pi z)$, the boundary conditions to accompany (5.1a,b) are

$$\tilde{u} = 0, \quad \tilde{w}' = (AM)\pi^2 \quad \text{at} \quad \bar{r} = 1, \tag{5.1c,d}$$

$$\text{finiteness at } \bar{r} = 0. \tag{5.1e}$$

The choice for $T_D(z)$ was discussed in some detail in DS we note, and the sinusoidal profile was adopted due to some inherent advantages, in particular enabling an explicit (heat-conduction type) temperature approximation to be obtained. Unpublished full computational results have also confirmed that the qualitative structure of the flow is essentially unaffected by different choices for $T_D(z)$.

The system (5.1a–e) was solved numerically via an abridged version of the reduced-model numerical solver described above. Furthermore, the solutions were checked by means of a separate alternative semi-implicit iteration procedure. Figure 7 indicates the dependence of $\tilde{q}$ on AM, where non-uniqueness is clearly evident, as well as the anticipated cut-off point for positive AM values. Another feature of interest is the branch behaviour for negative values of AM. Both branches appear to suggest that the pressure gradient eventually becomes large and negative, as AM is decreased towards certain critical values. An asymptotic analysis of the midzone system for $-\tilde{q} \gg 1$ given next, addresses this issue. The results obtained therein will be used in Section 6 to compare with computational results.

5.2 Large negative thermocapillary stresses

Here we attempt to determine solution properties of (5.1a–e) for large negative pressure. First, in order to have consistent dominant balances in the momentum and continuity equations, the relationships $u \sim w \sim (-q)^{1/2}$ would appear to be necessary. This leads to the following asymptotic expansions:

$$\tilde{u} = \hat{\alpha}\tilde{u}_0 + \hat{\beta}\tilde{u}_1 + \cdots, \ \tilde{w} = \hat{\alpha}\tilde{w}_0 + \hat{\beta}\tilde{w}_1 + \cdots, \ \tilde{q} = \hat{\alpha}^2\tilde{q}_0 + \hat{\beta}\tilde{q}_1 + \cdots, \tag{5.2}$$

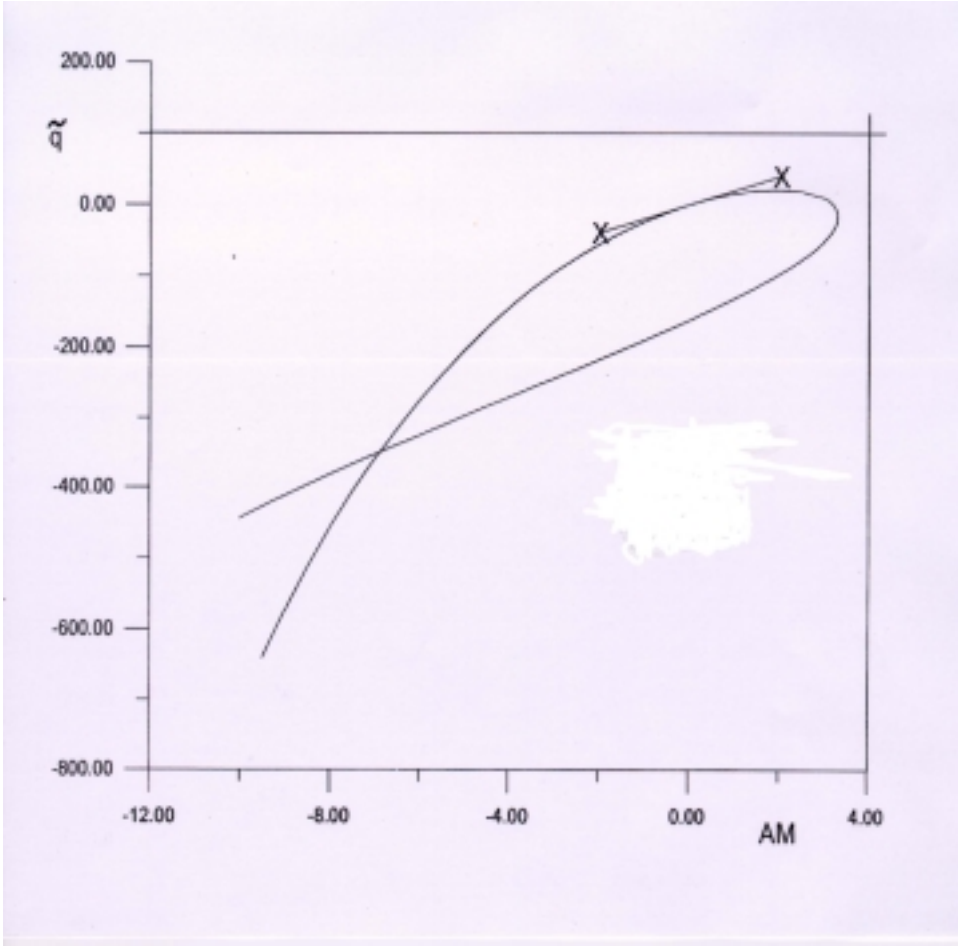

Figure 7: Midzone-analysis result for $\tilde{q}$ vs. AM. The lubrication results is indicated for comparison, by crosses.

where $\hat{\alpha} \gg 1$ and $\hat{\beta} \ll \hat{\alpha}$. Before investigating further, it is convenient here to eliminate w from the nonlinear terms in (5.1b). Using the continuity equation for this purpose, it follows that:

$$-\tilde{u}\tilde{u}'' + \tilde{u}'^2 + \tilde{u}\tilde{u}'/\bar{r} + 2\tilde{u}^2/\bar{r}^2 = -\tilde{q} + (\bar{r}\tilde{w}')'/\bar{r}. \tag{5.3}$$

Substituting (5.2) into (3.3) yields, to leading-order, the nonlinear-inviscid equation

$$-\tilde{u}_0\tilde{u}_0'' + \tilde{u}_0'^2 + \tilde{u}_0\tilde{u}_0'/\bar{r} + 2\tilde{u}_0^2/\bar{r}^2 = -\tilde{q}_0, \tag{5.4}$$

which is valid for $0 < \bar{r} < 1$. From the coordinate change $s = \bar{r}^2$ we can deduce that

$$2s(2\tilde{u}_0\tilde{u}_{0ss} - 2\tilde{u}_{0s}^2 - \tilde{u}_0^2/s^2) = \tilde{q}_0. \tag{5.5}$$

By letting $u_0 = \tilde{u}_0 s^{1/2}$ this simplifies further to

$$4(u_0 u_{0ss} - {u_{0s}}^2) = \tilde{q}_0. \tag{5.6}$$

Although (5.6) admits several types of solutions, we would expect at least one or other of the boundary conditions at the slip and axis to hold, and preferably both. Hence, for example, while (5.6) admits a solution proportional to $\pm\sinh(c_1 s + c_2)$ for any real c_2, and nonzero real c_1, this would in turn imply a radial velocity profile like $\sinh(c_1\bar{r}^2 + c_2)/\bar{r}$, and only one of (5.1c) or

(5.1e) and not both can be fulfilled. An alternative solution form to (5.6) is $\sin(c_1 s + c_2)$, so that $\tilde{u}_0 = \pm\gamma \sin(c_1\bar{r}^2 + c_2)/(c_1\bar{r})$, again for real c_1, c_2 with $c_1 \neq 0$ and with (real) $\gamma = (-\tilde{q}_0/4)^{1/2}$ (which is consistent with the negative pressure gradient, we note). By limiting c_1 to the set $\{n\pi : n \in \mathbb{N}\}$ and setting $c_2 = 0$ we can now satisfy the boundary conditions for $\tilde{u}_0$ at both the axis and the slip. Hence, one set of possible solutions is:

$$\tilde{u}_0 = \pm\gamma \sin(n\pi\bar{r}^2)/(n\pi\bar{r}), \quad (n \in \mathbb{N}) \tag{5.7a}$$

and from (5.1a) it then follows immediately that

$$\tilde{w}_0 = \mp 2\gamma \cos(n\pi\bar{r}^2), \quad (n \in \mathbb{N}). \tag{5.7b}$$

While $\tilde{w}_0$ is consistent with the finiteness condition at the axis, we cannot directly satisfy the stress condition on the slip, since $\tilde{w}_0' = 0$ there. This suggests we need to consider higher order effects, in order to accommodate (5.1d). It is reasonable to expect a viscous correction effect at the next significant level, since we would otherwise obtain an essentially identical system to the leading-order one, and therefore be unable to fulfil (5.1d). Hence, balancing terms in (5.3) suggests that $\beta = O(1)$ and

$$-\tilde{u}_0\tilde{u}_1'' - \tilde{u}_1\tilde{u}_0'' + 2\tilde{u}_0'\tilde{u}_1' + \tilde{u}_0\tilde{u}_1'/\bar{r} + \tilde{u}_1\tilde{u}_0'/\bar{r} + 4\tilde{u}_0\tilde{u}_1/\bar{r}^2 = -\tilde{q}_1 + R_n, \tag{5.8}$$

where

$$R_n = \pm 8\gamma n\pi(\sin(n\pi\bar{r}^2) + n\pi\bar{r}^2\cos(n\pi\bar{r}^2)) \tag{5.9}$$

denotes the viscous-correction term.

The solution properties of (5.8) are examined in detail in Appendix B, but here we just note the salient points: firstly, we can derive a solution for $\tilde{u}_1$ which satisfies the axis and slip conditions (i.e. is zero-valued there) and secondly, a corresponding solution for $\tilde{w}_1$ which satisfies the axis condition. At the approach to the slip ($\bar{r} \to 1^-$), we obtain the interesting result:

$$\tilde{w}_1 \sim -16n^2\pi^2 + O[(1-\bar{r})\log(1-\bar{r})]. \tag{5.10}$$

In order that (3.10) is compatible with the stress condition on the slip, it is therefore necessary that

$$(AM)_n = 16n^2, \tag{5.11}$$

where $(AM)_n$ denotes the cut-off value corresponding to the n'th solution of (5.7a,b), as $\tilde{q} \to -\infty$.

6 Numerical results for $Ma < 0$

Although flows with negative Marangoni number are perhaps less applicable in practice, at the very least they provide us here with a good opportunity to validate full numerical solutions against reduced-model computations and associated asymptotic theory. In the slender-flow model, the lubrication solution approximation of DS, which in scaled form is

$$u_L = \frac{\pi^2\bar{r}}{8}\left(1-\bar{r}^2\right)\sin(\pi z), \qquad w_L = \frac{\pi}{4}\left(1-2\bar{r}^2\right)\cos(\pi z), \qquad p_L'(z) = -2\pi\cos(\pi z), \tag{6.1a-c}$$

and holds in the bulk of the domain, is known to be appropriate on the attractor branch (but not the other - see Figure 7) for small values of $|AM|$; moreover as DS demonstrated for positive values of AM, these solutions are remarkably robust and continue to serve as a good approximation in much of the domain (i.e. away from the end-walls) even for $O(1)$ values of $|AM|$.

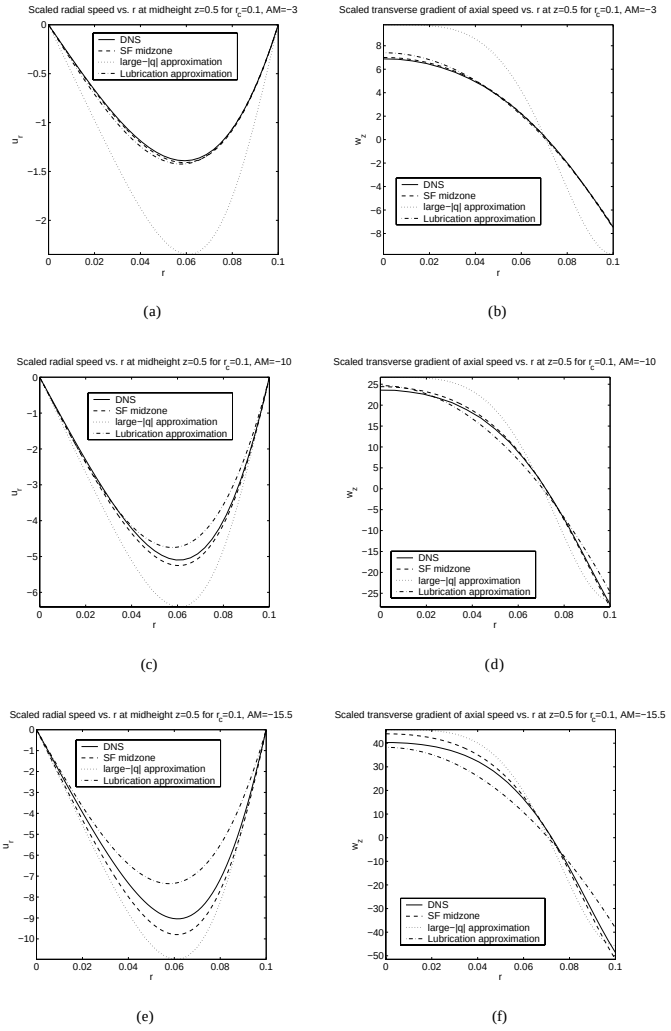

Figure 8: Narrow-domain full simulation for $Pr = 0.01$, $rc = 0.1$ depicting the radial profiles at z=0.5 for the radial velocity component and the axial velocity gradient respectively in (a),(b) for AM=-3; (c),(d) for AM=-10; (e),(f) for AM=-15.5. In each case comparisons are made with computed slender-flow data, an approximate lubrication solution and (5.7a,b) with n=1.

It has also been shown in Section 5.2 above that possible theoretical approximations exist in the midzone of the domain (around $z = 0.5$) in the limit of large negative pressure. In this section these predictions are tested against full numerical solutions, as well as the numerical solutions provided by the slender-flowl finite-difference midzone solver described above (and more extensively in DS). For the full simulations, the Prandtl number has the value 0.01 while the dimensionless cylinder radius is taken as 0.1.

Figure 8 shows the comparison of the numerical results with the lubrication solution and the solution (5.7a,b) for $n = 1$. Here the comparisons are for radial velocity and axial velocity gradient at the midzone; the first plots for $AM = -3$ confirms the point made about the robustness of the lubrication solution, while the plots for $AM = -10$ and $AM = -15.5$ show the increasing relevance of the given limiting solution for large $-|q|$. It seems fully reasonable to expect that none of the other possible integer values in (5.7a,b) will give a more accurate solution, since for example, both full and reduced computational solutions indicate that the radial velocity has no

intermediate zeroes in (0,1), whereas it's easy to see that the n'th solution in (5.7a,b) has exactly $(n-1)$ intermediate zeroes. A global view of the solution is given in Figure 9, where the basic qualitative form of the solution can be seen: here the solution consists of two counter-rotating vortices of equal size with common axis $r = 0$, as with the steady 2D qualitative form for positive values of AM; an example of the latter is also shown in this figure for convenience. We see that the solution forms are similar, with the major exception being that, for $AM < 0$ the solution consists of *inward-flowing* motion along the midzone, i.e .the direction of motion in each vortex is reversed compared to the situation for $AM > 0$.

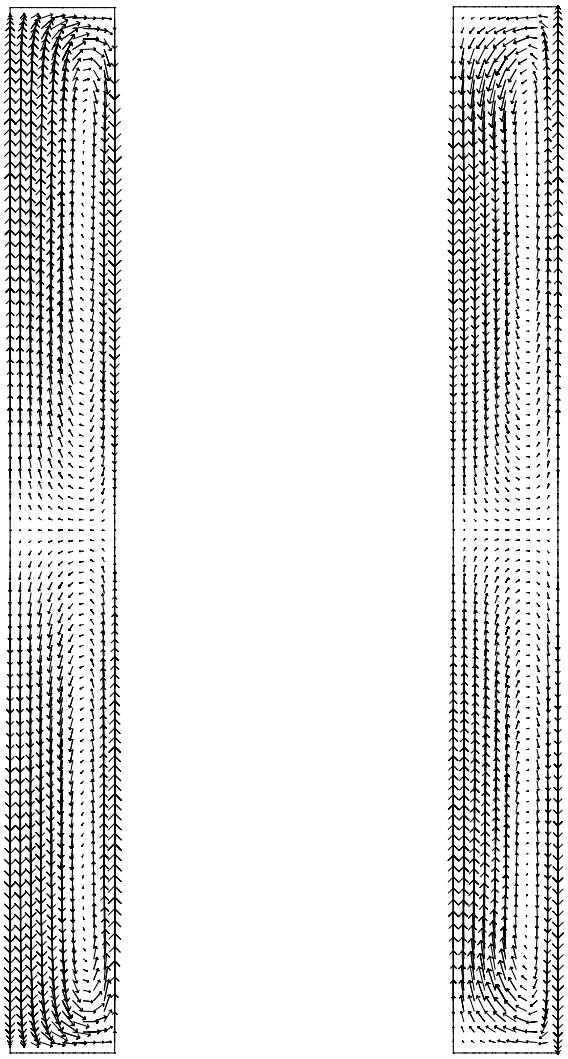

(a) (b)

Figure 9: Computed velocity field in a narrow domain for $Pr = 0.01$, $rc = 0.1$ with (a) $AM = -10$; (b) $AM = 2$.

If we assume now that the solution (5.7a,b) with $n = 1$ is a valid midzone approximation to upper branch solutions, then according to (5.11) we should expect the upper-branch slender-flow solution to cut-out at $AM = -16$. Reduced-model computations have directly confirmed this feature,

with no accurate solutions being computable below this value. Full axisymmetric solutions were computed for AM values as low as -25 however, and several interesting features were uncovered. In Figure 10 the radial and axial velocity profiles at $r = 0.05$ are plotted. We are especially interested in the behaviour of the former, where the focus is on the convexity of the curves; as Figures 10c,d suggest, the curves for $AM > -16$ are entirely convex in the bulk of the domain (i.e. excluding the high-shear behaviour near the endwalls, where the slender-flow approximation is not valid). In contrast, for $AM < -16$, the curves are clearly non-convex, while at $AM = -16$ the associated curve exhibits two points of inflection (roughly), while otherwise being convex in nature. This result exactly mirrors the findings for positive AM described in DS, and seems to suggest strongly that the two-dimensional steady state is lost once the radial profile exhibits a point of inflection in the bulk. Unfortunately, we cannot provide any mathematical evidence to support this, although of course, it's well-known that inflectional profiles are often linked to the onset of instabilities.

Finally here, we remark that some effort was made to better understand the nature of the lower branch, in particular whether or not the branch there also cuts out at a finite value, or perhaps exhibits some other trend, such as exponential growth. No firm conclusions could be made however, partly due to the associated difficulty of obtaining a converged and valid solution on this branch, even using the reduced-model code. From those solutions successfully computed however, the solution form for the radial velocity suggested that the theoretical approximation (5.7a,b) with $n = 2$ might possibly hold, especially as the former consistently yielded one intermediate zero in $(0, 1)$; corresponding plots depicting the behaviour of the axial velocity gradient were less convincing however, and so no firm conclusions can be made here.

7 Conclusions

In the preceding sections we have studied the flow behaviour of thermocapillary-driven liquid bridges for both positive and negative Marangoni number.

For positive Marangoni number, where the motion on the liquid-gas interface is outward directed (and inward along the axis), full computations for $rc = 0.5$ have demonstrated that steady axisymmetric flow first becomes unstable to the azimuthal mode $m = 2$. Hence, this mode is the most dangerous in a 'linear' sense, and furthermore is stationary in nature, exactly in agreement with half-zone predictions for this same test case (Wanschura et al 1995). We are also concerned however with possible mode development and interaction, and therefore compute for relatively large end-times; this enables us for instance to witness the later activation of the $m = 1$ mode, and its subsequent interplay with other modes, particularly the $m = 0$ and $m = 2$ modes. It is clear from the frequency table in Section 4 and Figures 2, 3 that the modes $m = 1$ and $m = 2$ are nonlinearly related due to the evident frequency doubling. The above computations were performed with $Pr = 0.02$, although we note that the instability here is virtually independent of Pr, provided that $Pr \ll 1$, as for half zones (Wanschura et al 1995).

While no exact prediction for the critical dynamic Reynolds number Re_D^* can be made for the given test case, our numerical results indicate that $Re_D \in (2400, 2500)$. As $(Re_D - Re_D^*)$ increases, the relative importance of the $m = 2$ mode decreases and $m = 1$ begins to dominate alone; loosely speaking, the greater the dominance of the latter mode, the greater the loss of mirror symmetry in vertical plane plots, as can be observed in Figures 4,6, for example.

For negative Marangoni number the slender-flow midzone analysis of DS (also Figure 7 here) suggest that the pressure becomes large and negative at the approach to a finite, critical value

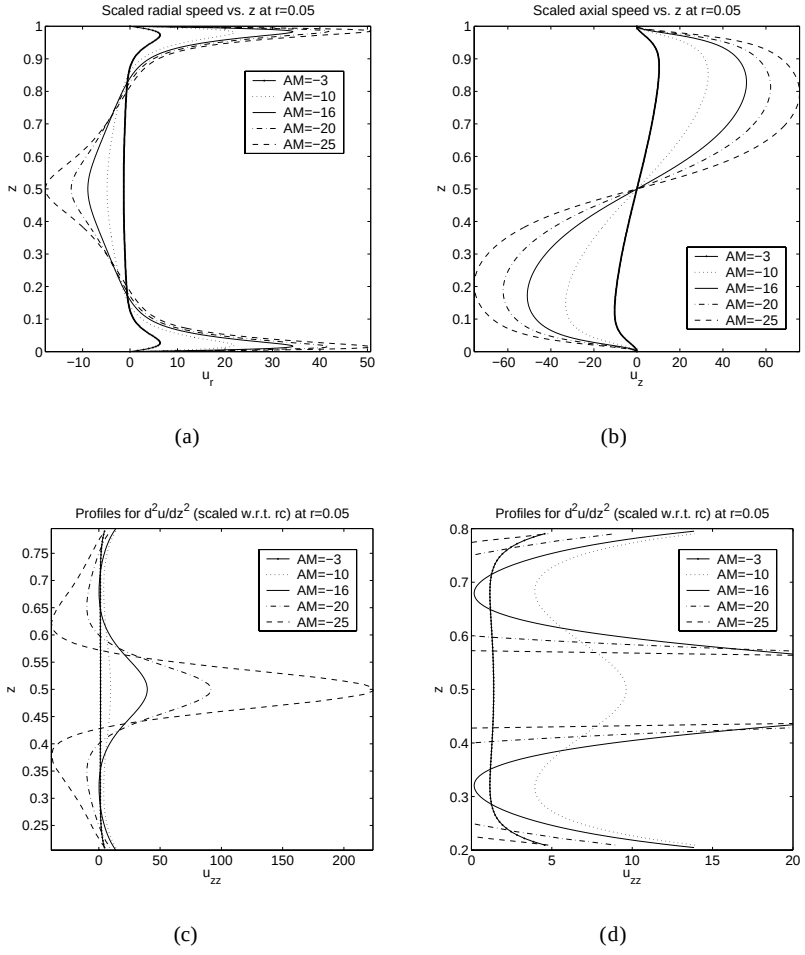

Figure 10: Full computational results for $AM = -3,\ -10,\ ,-16,\ -20,\ -25$ indicating (a) the scaled radial velocity component; (b) the scaled axial velocity component vs. z at $r = 0.05$. In (c) the double axial derivative of the former is shown, and in (d) a close-up focussing on inflectional properties.

of AM. The asymptotic analysis presented in Section 5.2 assumes a mainly inviscid response in the midzone, and while regular solutions can be obtained, e.g. (5.7a,b), the thermocapillary stress condition cannot be satisfied at this level. Instead higher-order viscous effects need to be taken into account, and consequently the n'th solution of (5.7a,b) is valid only if $AM \approx (AM)_n$, where $(AM)_n = -16n^2$. Both full and slender-flow midzone computational results of upper branch cases are compared with *the* $n = 1$ *solution* of (5.7a,b), as well as the lubrication approximation of DS; very good agreement with the latter is shown for $AM = -3$, while the agreement with the former improves markedly as AM is reduced further, with fairly good agreement evident for $AM = -15.5$.

Finally we remark once again on the 'lemonhead' effect, first described in DS. In that study, the radial velocity exhibited non-convex profiles across the midzone for $AM > AML(\approx 3.3108)$. In Figure 10b we see an analogous situation for $AM < -16$. Moreover, Figures 10c,d infer that the critical value corresponds to the first instance where the profile is not completely convex, but has at least one point of inflection (two in our case, due to midheight symmetry).

Acknowledgements

Thanks are due to Prof. E. Bänsch for providing the fundamental components of the finite-element

solver.

Appendix A. Stress-Curvature-Torsion (SCT) Boundary-Integral Form

Taking the $L_2(\Omega)$ scalar product of (2.2a), we integrate the diffusion part using Green's Theorem directly, i.e.

$$-\int_{\Omega}(\Delta\mathbf{u}\cdot\boldsymbol{\phi})\,d\mathbf{x} \;=\; \int_{\Omega}(\nabla\boldsymbol{\phi}\;:\;\nabla\mathbf{u})d\mathbf{x} - I_{\Gamma}, \tag{A1}$$

where

$$I_{\Gamma} := \int_{\Gamma_{LG}} \frac{\partial \boldsymbol{u}}{\partial n}\cdot\boldsymbol{\phi}\;ds. \tag{A2}$$

If we suppose that $(\boldsymbol{\tau}_1, \boldsymbol{\tau}_2, \mathbf{n})$ is an orthonormal basis of $\mathbb{R}^3$, where $\boldsymbol{\tau}_1, \boldsymbol{\tau}_2$ are vectors in the local tangent plane on Γ_{LG} and $\mathbf{n}$ is the local outer normal, then generalising (2.2f) to include any right-hand side (continuous on Γ_{LG}) we have the two independent boundary conditions

$$\boldsymbol{\tau}_i\cdot(\sigma\mathbf{n}) \equiv \mathbf{n}\cdot\sigma\boldsymbol{\tau}_i = g_i \;\text{ on }\; \Gamma_{LG}, \tag{A3}$$

for i=1,2.

Clearly, only the 'strain' part of σ makes a contribution here, and hence, for $i = 1, 2$ on Γ_{LG}

$$g_i = \boldsymbol{\tau}_i\cdot[(\nabla\mathbf{u})\mathbf{n}] + \boldsymbol{\tau}_i\cdot[(\nabla\mathbf{u})^{\mathrm{T}}\mathbf{n}], \tag{A4}$$

which reduces to

$$g_i = \boldsymbol{\tau}_i\cdot\frac{\partial\mathbf{u}}{\partial n} + \mathbf{n}\cdot\frac{\partial\mathbf{u}}{\partial\tau_i} \tag{A5}$$

using associativity arguments.

Since $(\boldsymbol{\tau}_1, \boldsymbol{\tau}_2, \mathbf{n})$ is an orthonormal basis, and using the non-deformation condition on Γ_{LG} in advance, we may write

$$\mathbf{u} = (\mathbf{u}\cdot\boldsymbol{\tau}_1)\boldsymbol{\tau}_1 + (\mathbf{u}\cdot\boldsymbol{\tau}_2)\boldsymbol{\tau}_2, \quad on \quad \Gamma_{LG}. \tag{A6}$$

Likewise,

$$\boldsymbol{\phi} = (\boldsymbol{\phi}\cdot\boldsymbol{\tau}_1)\boldsymbol{\tau}_1 + (\boldsymbol{\phi}\cdot\boldsymbol{\tau}_2)\boldsymbol{\tau}_2, \quad on \quad \Gamma_{LG}. \tag{A7}$$

Now combining (A5) and (A7), we can deduce that

$$\frac{\partial\boldsymbol{u}}{\partial n}\cdot\boldsymbol{\phi} = \sum_{i=1}^{2}(\boldsymbol{\phi}\cdot\boldsymbol{\tau}_i)g_i - \sum_{i=1}^{2}(\boldsymbol{\phi}\cdot\boldsymbol{\tau}_i)(\mathbf{n}\cdot\frac{\partial\mathbf{u}}{\partial\tau_i}). \tag{A8}$$

Since $\partial(\mathbf{u}\cdot\mathbf{n})/\partial\tau_i = 0$, for $i = 1, 2$, it follows from (A6) that

$$\mathbf{n}\cdot\frac{\partial\mathbf{u}}{\partial\tau_i} = \sum_{j=1}^{2}(\mathbf{u}\cdot\boldsymbol{\tau}_j)(\mathbf{n}\cdot\frac{\partial\boldsymbol{\tau}_j}{\partial\tau_i}). \tag{A9}$$

From elementary differential geometry it is easy to prove that

$$\frac{\partial\boldsymbol{\tau}_i}{\partial\tau_i} = -\kappa_i\mathbf{N}_i, \quad (i = 1, 2) \tag{A10}$$

where $\mathbf{N}_i$ denotes the outer normal for the i'th curve on Γ_{LG} and κ_i its curvature.

It can also be shown that

$$\frac{\partial \boldsymbol{\tau}_j}{\partial \tau_i} = -\rho_{ij}\mathbf{n} + \kappa_i(\mathbf{N}_i \cdot \boldsymbol{\tau}_j)\boldsymbol{\tau}_i, \tag{A11}$$

for $i = 1, 2$ with $j \neq i$, where ρ_{ij} denotes the normal torsion component of the vector $\boldsymbol{\tau}_j$ along the local coordinate τ_i.

Hence, combining (A8) – (A11) with (A2) we can determine that

$$I_\Gamma = \sum_{i=1}^{2} \int_{\Gamma_{LG}} (\boldsymbol{\phi}\cdot\boldsymbol{\tau}_i) g_i \, ds + \sum_{i=1}^{2} \int_{\Gamma_{LG}} (\boldsymbol{\phi}\cdot\boldsymbol{\tau}_i)(\mathbf{u}\cdot\boldsymbol{\tau}_i)(\mathbf{n}\cdot\mathbf{N}_i)\kappa_i \, ds + \sum_{i=1}^{2} \int_{\Gamma_{LG}} (\boldsymbol{\phi}\cdot\boldsymbol{\tau}_i)(\boldsymbol{\phi}\cdot\boldsymbol{\tau}_{(3-i)})\rho_i \, ds, \tag{A12}$$

where, for convenience, we have dropped the 'j' subscript in the torsion term. This expression defines the *stress-curvature-torsion* form for I_Γ.

Finally, if we just restrict ourselves to normal sections (so that $\mathbf{N}_i = \mathbf{n}$), and moreover to *lines of curvature*, (that is, those unique curves yielding maximum and minimum curvature, which by necessity are orthogonal), we can further simplify the expression to

$$I_\Gamma = \sum_{i=1}^{2} \int_{\Gamma_{LG}} (\boldsymbol{\phi} \cdot \boldsymbol{\tau}_i) g_i \, ds + \sum_{i=1}^{2} \int_{\Gamma_{LG}} (\boldsymbol{\phi} \cdot \boldsymbol{\tau}_i)(\mathbf{u} \cdot \boldsymbol{\tau}_i)\kappa_i \, ds. \tag{A13}$$

Here we have used an elementary property of differential geometry, namely zero torsion along lines of curvature. (This can be easily visualised for axisymmetric surfaces – such as our cylindrical domain – where the lines of curvature are the meridians and parallels; these curves are clearly planar, and hence yield zero torsion.)

Appendix B. Properties of the viscous-correction system

The proposed leading-order solutions (5.7a,b) for $-\tilde{q} \gg 1$ automatically result in zero shear stress on the slip, and hence, this condition must be accommodated at a higher order. The first non-trivial change we can expect is when viscous effects are taken into account.

We first write $\tilde{u}_1 = \tilde{u}_0 \, \phi$ in (5.8) resulting in:

$$\tilde{u}_0^2(\phi'' - \phi/\bar{r}) + 2\tilde{q}_0\phi = \tilde{q}_1 - R_n, \tag{B1}$$

where $'$ denotes differentiation with respect to $\bar{r}$, as in Section 5.2. Here the properties of $\tilde{u}_0$ have been exploited to reduce the complexity on the left-hand side. Making the variable switch $t = n\pi\bar{r}^2$ allows us to further simplify the form of the relationship to

$$\sin^2(t)\phi_{tt} - 2\phi = -(\tilde{q}_1/\tilde{q}_0) \pm 8\gamma n\pi(\sin(t) + t\cos(t)). \tag{B2}$$

A second substitution $\phi = \psi\cot(t)$ enables us to derive the equation

$$(\cot^2(t)\psi_t)_t = -(\tilde{q}_1/\tilde{q}_0)\cot(t)\csc^2(t) \pm (8\gamma n\pi/\tilde{q}_0)\cot(t)\csc^2(t)(\sin(t) + t\cos(t)), \tag{B3}$$

which upon integration yields

$$\psi_t = (\tilde{q}_1/2\tilde{q}_0)\sec^2(t) \mp (4\gamma n\pi/\tilde{q}_0)[t/\cos(t) + \tan^2(t)\int^t \hat{t}\csc(\hat{t}) \, d\hat{t} + 3\sec(t)\tan(t)] + D_1\tan^2(t). \tag{B4}$$

Here the bar on the integral sign denotes the principal value. A final integration gives

$$\psi = (\tilde{q}_1/2\tilde{q}_0)\tan(t) \mp (4\gamma n\pi/\tilde{q}_0)[(\tan(t)-t)\fint^t \hat{t}\csc(\hat{t})\,d\hat{t} + \fint^t \hat{t}^2\csc(\hat{t})\,d\hat{t} + 3\sec(t)] + D_1(\tan(t)-t) + D_2. \tag{B5}$$

Here we note that D_1 and D_2 are constants of integration, and these can be determined uniquely by imposing the radial-velocity conditions of finiteness at the axis and zero-valuedness at the slip. Subsequently, we have the properties $\psi \sim t$ as $t \to 0^+$ and $\psi \sim (n\pi - t)$ as $t \to 1^-$.

It is clear from second order in the continuity equation that $\tilde{w}_1$ satisfies

$$\tilde{w}_1 = -\tilde{u}_1' - \tilde{u}_1/\bar{r}. \tag{B6}$$

With the substitution $\tilde{u}_1 = \tilde{u}_0\phi$ and an identical relationship to (B6) for $\tilde{u}_0$, $\tilde{w}_0$ stemming from leading-order continuity balances, it immediately follows that

$$\tilde{w}_1 = \tilde{w}_0\phi - \tilde{u}_0\phi'. \tag{B7}$$

Owing to the asymptotic nature of ψ at the axis, it follows that ϕ is bounded there, while $\phi' \sim t^{-1/2}$ there; since $\tilde{u}_0 \sim t^{1/2}$ and $\tilde{w}_0 \sim 1$ clearly follow from (5.7a,b) we can conclude that $\tilde{w}_1$ is finite at the axis. It remains to examine the shear stress contribution at the slip. Differentiating $\tilde{w}_0$ with respect to $\bar{r}$ in (B6), and combining the result with (B1) yields

$$\tilde{w}_1' = (\tilde{w}_0' + 2\tilde{q}_0/\tilde{u}_0)\phi + 2\tilde{w}_0\phi' - \tilde{q}_1/\tilde{u}_0 + R_n/\tilde{u}_0. \tag{B8}$$

Substituting for ϕ again, we can determine with the aid of (5.7a,b) that

$$\tilde{w}_1' = \pm 4\gamma(\pi t)^{1/2}[\psi\cos(t) - 2\psi_t\cot(t)\csc(t) + (R_n - \tilde{q}_1)\csc(t)/(4\gamma^2)]. \tag{B9}$$

Then combining (5.9) and (B4), and noting that $\psi(n\pi) = 0$, it follows that

$$\tilde{w}_1' \sim -16n^2\pi^2 + O[(1-\bar{r})\log(1-\bar{r})], \tag{B10}$$

as $\bar{r} \to 1^-$.

References

BÄNSCH, E. 1998 Simulation of instationary, incompressible flows. *Acta Math. Univ. Comenianae* **LXVII**, 101–114.

BRISTEAU, M. O., GLOWINSKI, R. & PERIAUX, J. 1987 Numerical methods for the Navier–Stokes equations. Applications to the simulation of compressible and incompressible flows. *Computer Physics Report* **6**, 73–188.

CHUN, C.–H. & WUEST, W. 1979 Experiments on the transition from steady to oscillatory Marangoni convection in a floating zone under reduced gravity effect. *Acta Astronautica* **6**, 1073–1082.

CRÖLL, A., MÜLLER-SEBERT, W., BENZ, K. W. & NITSCHE, R. 1991 Natural and thermocapillary convection in partially confined silicon melt zones. *Microgravity Sci. Technol. III* **4**, 204–215.

DAVIS, S. H. 1987 Thermocapillary instabilities. *Ann. Rev. Fluid Mech.* **19**, 403–435.

DAVIS, D. & BÄNSCH, E. 2002 An operator-splitting finite-element approach to the 8:1 thermal cavity problem. *Int J Numer Meth Fluids* **40**, 1019–1030.

Davis, D. A. R. & Smith, F. T. 2003 Flow and thermal convection in full-zone liquid bridges of wide-ranging aspect ratio. *Theoret. Comput. Fluid Dynamics* **17**, 113–146.

Eyer, A., Leiste, H. & Nitsche, R. 1985 Floating zone growth of silicon under microgravity in a sounding rocket. *J. Crystal Growth* **71**, 173–182.

Gresho, P. M. & Sani, R. L. 2000 *Incompressible flow and the finite element method. Vol. 2: Isothermal laminar flow.* Wiley, Chichester, England.

Hu, W.–R., You, H.–T. & Cao, Z.–H. 1992 Free surface oscillation of thermocapillary convection in liquid bridge of half-floating zone. *Sci. China A* **35**, 1101.

Jurisch, M. & Löser, W. 1990 Analysis of periodic non-rotational W striations in Mo single crystals due to nonsteady thermocapillary convection. *J. Crystal Growth* **102**, 214–222.

Kaiser, T. & Benz, K. W. 1998 Floating-zone growth of silicon in magnetic fields, Part III: numerical simulation. *J. Crystal Growth* **191**, 365–376.

Levenstam, M. & Amberg, G. 1995 Hydrodynamical instabilities of thermocapillary flow in a half-zone *J. Fluid Mech.* **297**, 357–372.

Leypoldt, J., Kuhlmann, H. C. & Rath, H. J. 2000 Three-dimensional numerical simulation of thermocapillary flows in cylindrical liquid bridges. *J. Fluid Mech.* **414**, 285–314.

Preisser, F., Schwabe, D. & Scharmann, A. 1983 Steady and oscillatory thermocapillary convection in liquid columns with free cylindrical surface. *J. Fluid Mech.* **126**, 545–567.

Wanschura, M., Shevtsova, V. M., Kuhlmann, H. C. & Rath, H. J. 1995 Convective instability mechanisms in thermocapillary liquid bridges. *Phys. Fluids* **7**(5), 912–925.

Widnall, S. & Tsai, C.–Y. 1977 The instability of the thin vortex ring of constant vorticity. *Proc. R. Soc. Lond. A* **287**, 273–305.